

# Control of Nanoscale Heat Generation with Lithography-Free Metasurface Absorbers

Jon W. Stewart, Tamra Nebabu, and Maiken H. Mikkelsen\*



Cite This: *Nano Lett.* 2022, 22, 5151–5157



Read Online

ACCESS |



Metrics & More



Article Recommendations

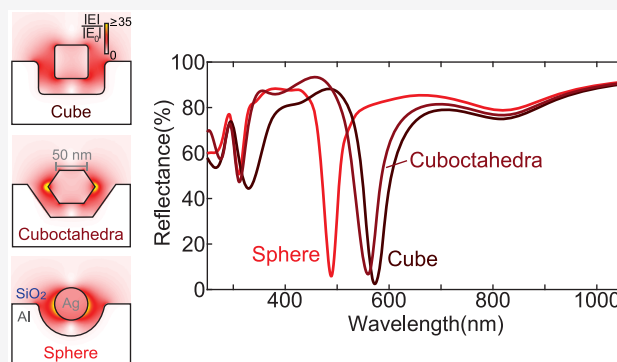


Supporting Information

**ABSTRACT:** Metasurfaces, artificially engineered surfaces comprised of subwavelength resonators, show promise for realizing a new generation of optical materials and devices. However, current metasurface architectures suffer from environmental degradation, a limited spectral range, and a lack of scalability. Here, we demonstrate a novel large-area embedded metasurface architecture that is environmentally robust and capable of a spectrally selective absorption of greater than 80% spanning from 330 to 2740 nm. These fully encapsulated metasurfaces leverage the capabilities of colloidal plasmonic nanoparticles with various crystallinities, materials, shapes, and sizes to access a larger spectral range and allow for control of nanoscale spatial losses and subsequent heat generation within the constituent elements of the metasurface.

Through the selection of material, particle size, and shape, these metasurfaces can be designed across the ultraviolet (UV) to short-wave infrared (SWIR) region for various hot-electron, photodetection, photocatalysis, and photothermal processes.

**KEYWORDS:** *plasmonic metasurfaces, colloidal self-assembly, spectrally selective, nanoscale heat generation, perfect absorber*



Metasurfaces are artificial materials or surfaces comprised of an ensemble of subwavelength elements, allowing for unparalleled control of electromagnetic waves that circumvent the limitations of naturally occurring optical materials. For specific applications, light absorption and subsequent energy conversion is essential, but naturally occurring materials in the UV to SWIR region have limited absorption ranges corresponding to inherent electron and phonon excitations. Metamaterials, on the other hand, can be designed to realize high-efficiency absorption for nearly any wavelength by taking advantage of metallic nanostructures.<sup>1–5</sup> Light incident upon the metallic nanostructures excites localized surface plasmons: i.e., coherent oscillations of free electrons confined to the surface of a highly conductive material. These plasmons are resonant oscillations that are dependent on the geometry and materials of the metallic nanostructures and as such are well-suited for designable metamaterials. When they are packed to a specific surface density, the collective electric and magnetic response can destructively interfere with incident radiation, resulting in near-perfect absorption at the plasmon resonance.<sup>6,7</sup> Typically, these large electric and magnetic modes are achieved through coupling two planar plasmonic surfaces to create a plasmonic cavity<sup>8,9</sup> and are realized by separating nanoscale disks or cubes from a smooth metallic film with a dielectric spacer. Achieving resonances in the UV to SWIR region with these plasmonic nanocavities requires a specialized fabrication to achieve relevant feature sizes that are less than 300 nm.<sup>10,11</sup> Top-down approaches, such as deep-UV or electron-beam lithography, are

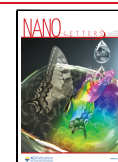
capable of achieving sub 10 nm feature sizes but are either prohibitively expensive or not capable of patterning over wafer-scale areas. Bottom-up synthesis approaches are capable of growing large quantities of metallic nanoparticles with planar facets and monodisperse sizes but necessitate a crystalline growth process that can limit the size and material selection.<sup>2</sup> Lithography-free approaches such as planar metasurfaces have shown spectrally selective absorbing surfaces from the visible to midwave infrared region<sup>12–17</sup> but lack full spatial control over the absorbed power and heat generation. As such, no current metasurface platform has been capable of producing strongly absorbing filters that span the UV to SWIR region over large areas, while allowing for the spatial losses, heat, or hot-electron generation to be fully designed for a chosen application.

Here we demonstrate a new metasurface architecture that can realize absorbing metasurfaces ranging from 330 to 2740 nm over wafer-scale areas through the utilization of standard colloidal synthesis, material growth, and deposition techniques. Due to the stochastic self-assembly process of the colloidal deposition, the metasurfaces are comprised of randomly

**Received:** March 1, 2022

**Revised:** June 7, 2022

**Published:** July 1, 2022



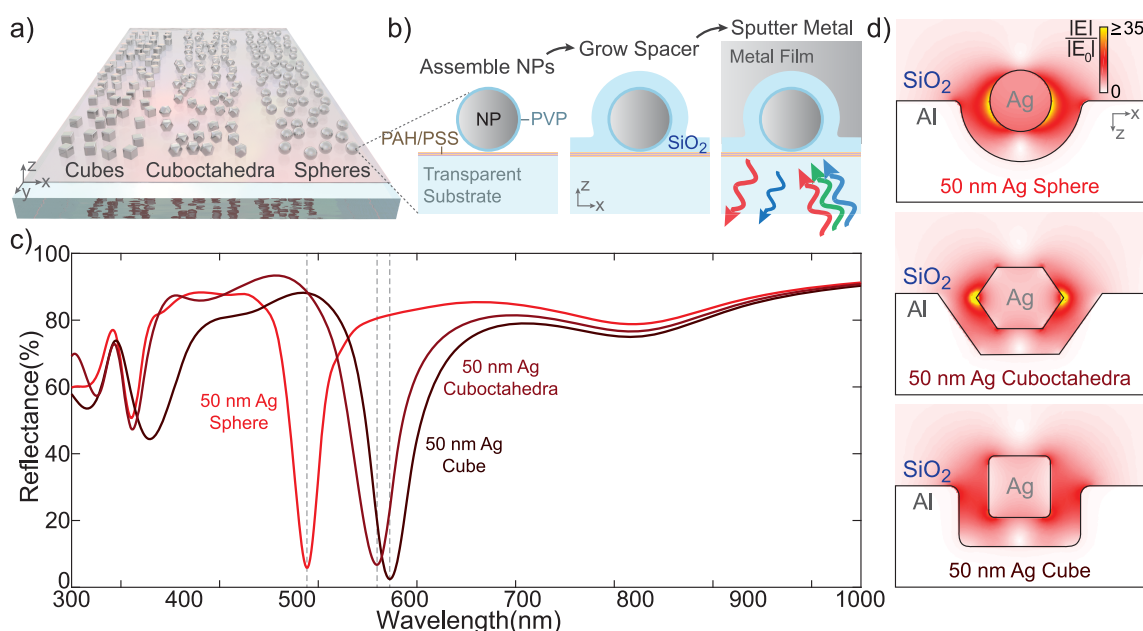


**Figure 1.** (a) Depiction of various colloidal nanoparticle (NP) shapes self-assembled onto a transparent substrate. (b) Process of fabricating a plasmonic metasurface shown with a single metasurface unit cell. First the NPs are self-assembled onto a transparent substrate, then a dielectric spacer such as  $\text{SiO}_2$  is grown around the NPs, and finally a metal film is sputtered around the dielectric-coated NPs to form a conformal plasmonic cavity around the NP. (c) Simulated reflection spectra for three metasurfaces comprised of the three NP shapes shown in (a), depicting that the wavelength of resonant absorption depends upon the geometry of the plasmonic cavity. (d) Simulated electric-field enhancement for the three metasurface elements at their resonant wavelengths, demonstrating the plasmonic coupling between the Ag NPs and the Al film.

oriented plasmonic nanocavities. These nanocavities support a localized surface plasmon resonance (LSPR) between two closely spaced plasmonic surfaces.<sup>2,4</sup> In this work, the plasmon resonance is passively controlled by varying the size, material, and geometry of the nanostructures. In order to fabricate plasmonic resonators with variously shaped nanoparticles (NPs), a new fabrication technique is developed in order to create two closely spaced metallic surfaces separated by a dielectric gap, as shown in Figure 1a. This fabrication approach incorporates NPs of different shapes that arise during colloidal synthesis and creates highly absorbing metasurfaces from NPs previously incapable of doing so.

This fabrication is initiated by conformally depositing the plasmonic NPs onto a substrate by coating the substrate in alternating PAH/PSS (cationic/anionic) polymer layers. The top cationic layer polymer facilitates an electrostatic self-assembly of the NPs coated with an anionic coating from their host solution, resulting in the first diagram of Figure 1b. Next, a dielectric coating is grown around the nanoparticles with plasma-enhanced chemical vapor deposition (PECVD) and then a metal film is physically sputtered around the dielectric-coated NP. By using a transparent substrate within the desired wavelength range, the light incident through the substrate will excite the plasmonic resonances between the NP and sputtered metal films, as shown in the last panel of Figure 1b. Finite-element simulations were used to model the optical response of the three different geometries with 50 nm NPs, a 24 nm  $\text{SiO}_2$  spacer, and a 150 nm Al film. A fill fraction of 12% was used for the 50 nm Ag spheres and 4% for the 50 nm Ag cubes and 50 nm cuboctahedra. The simulated reflectance spectra in Figure 1c show that the peak absorptivity at the fundamental plasmon resonance occurs at 575 nm for the cubic NPs, 560 nm for the cuboctahedral NPs, and 490 nm for the spherical NPs, as indicated by the gray dashed lines. The electric field enhance-

ment at the fundamental plasmon resonance for each of these geometries is included in Figure 1d. The electric field enhancement shows that the majority of the electric field is contained in and near the surfaces of the NP. This plasmon oscillation confined to the NP is coupled to an oscillation of the opposite phase in the sputtered metal film. This coupled mode between the NP and the film reduces or cancels the electric field in the far field, preventing reradiation of the incident energy, which results in the significant absorption of metasurfaces comprised of these elements.

Experimentally, the metasurfaces were realized following the procedure laid out in Figure 1b, and more details of the fabrication process are described in the experimental section in the Supporting Information. First, the NP shape dependence was tested experimentally with  $45 \pm 4$  nm Ag spheres and  $48 \pm 5$  nm Ag cubes, where the size distributions were calculated from SEM images. These NPs were self-assembled onto coverslips, and SEM images of both NPs assembled onto coverslips are shown in Figure 2a. Next, a  $\text{SiO}_2$  spacer layer was grown around the NPs, where the optimal absorption was achieved with a thickness of 30 nm or  $\sim 60\%$  of the NP size. Finally, a 150 nm thick Al film was sputtered and the reflection spectra were measured through the coverslip. Reflection spectra of the samples were collected with a Shimadzu UV-3600 commercial spectrometer at normal incidence and were integrated over an area with a 5 mm diameter. The reflection spectra from the 50 nm Ag sphere and cube metasurfaces are shown in Figure 2b along with a dimensionally labeled diagram. The Ag sphere metasurface has a peak absorption at 485 nm and possesses a 115 nm full width at half-maximum (fwhm), and the Ag cube metasurface possesses a peak absorption at 575 nm with a 195 nm fwhm. Finite-element simulations were used to estimate the reflection spectra of these metasurfaces, as shown in Figure 2c, and the optimal  $\text{SiO}_2$  thickness from simulations was found to be

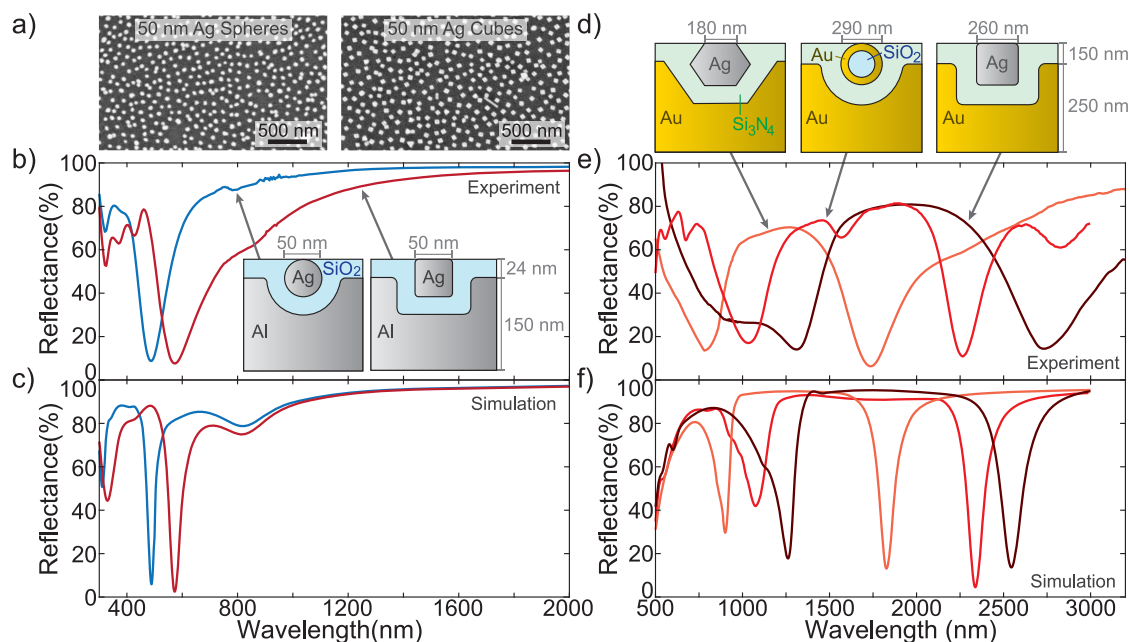


**Figure 2.** (a) SEM images of 50 nm Ag spheres and cubes assembled onto coverslips before growth of the SiO<sub>2</sub> spacer. (b) Experimental reflectance spectra for metasurfaces from the 50 nm Ag spheres and cubes shown in (a) along with labeled metasurface cross sections. (c) Simulated spectra for the metasurfaces created with 50 nm Ag spheres and cubes. (d) Three SWIR metasurface cross sections comprised of a 180 nm Au cuboctahedron, a 50 nm Au shell around a 200 nm silica core, and a 250 nm Ag cube. (e) Experimental reflectance spectra for these metasurfaces showing fundamental resonances in the SWIR and second-order resonances in the near-IR. (f) Simulated spectra of the three SWIR metasurfaces, closely following the spectral features of the experimental results.

~48% of the NP size, in contrast with the ~60% found experimentally. In comparison with the simulations of uniformly sized NPs, the experimental results possess increased fwhms due to the nonuniform size distribution of the colloidal NP solutions and a small number of NPs aggregating during deposition. The polycrystalline 50 nm Ag spheres have an  $\pm 8.9\%$  size deviation, and 90% of the NPs were unaggregated spheres after self-assembly, as determined from SEM images. The colloidal 50 nm Ag cubes possess a  $\pm 10.4\%$  size deviation where 91% of the NPs were unaggregated cubes after deposition. The fwhms can be improved through filtering the NP solutions for tighter size distributions. However, this metasurface platform is capable of producing highly absorbing metasurfaces with colloidal NPs of varying shapes and crystallinities with commercially obtained NP solutions.

To further establish the spectral flexibility of these metasurfaces, larger colloidal NPs were developed and synthesized (Nanocomposix Inc.) to realize resonances into the SWIR. Figure 2d shows three such metasurfaces with 180 nm Ag cuboctahedra, 45 nm Au shells around a 200 nm silica core, and 260 nm Ag cubes. The three metasurfaces consist of 108, 170, and 150 nm Si<sub>3</sub>N<sub>4</sub> spacers with a 250 nm sputtered Au film, and their experimental reflection spectra are shown in Figure 2e. Each spectrum shows a primary absorption peak in the SWIR at 1740, 2260, and 2740 nm corresponding to the fundamental plasmonic modes of the cuboctahedra, shell, and cube, respectively, whereas secondary absorption peaks exist in the near-IR at 780, 1030, and 1320 nm, respectively. Simulated reflection spectra from Figure 2f show fundamental modes at 1830, 2350, and 2540 nm with secondary modes at 900, 1080, and 1260 nm, which closely follow the experimental modes. Experimentally, the 290 nm Au shells show the narrowest fwhm of 260 nm due to the smaller 2.7% size distribution of the 288 nm shell NPs in comparison to the 6.6% and 6.5% distributions

of the 180 nm cuboctahedra and the 260 nm cubes, respectively. These results demonstrate that this versatile fabrication approach is clearly capable of achieving strongly absorbing surfaces from varying NP shapes, crystallinities, and materials while covering wavelengths from the visible to the SWIR region.

To further demonstrate the versatility of this approach, various metasurfaces were fabricated with resonances in the visible and UV regimes through utilization of smaller NPs and various plasmonic materials. These metasurfaces are comprised of 50 nm cubic or spherical NPs and plasmonic materials ranging from Al to Pt, Ag, and Au. Photographs of select metasurfaces were captured to show the large-area uniformity and color of these metasurfaces, which are shown in Figure 3a. For example, the top three metasurfaces Figure 3a-i–iii are 50 nm spherical NPs with a 30 nm SiO<sub>2</sub> layer and a 150 nm Al film where the NP material is (i) Pt, (ii) Ag, and (iii) Au. The reflectance spectra for these three metasurfaces are shown in Figure 3b along with their simulated spectra and a labeled schematic. The Pt metasurface shows a peak absorption at 330 nm, the Ag metasurface at 490 nm, and the Au metasurface at 575 nm. The peak absorptions for all possible combinations of Al, Pt, Ag, and Au films and 50 nm spherical NPs are shown in Figure 3c, which were obtained by finite-element simulations. With a fixed geometry, a variation of the constituent metasurface materials allows for a range of resonant wavelengths to be achieved. As such, the use of NPs with different materials, sizes, and shapes allow for the absorption spectra to be passively tuned across the ultraviolet to SWIR region with a single fabrication approach.

Beyond the wavelength flexibility of these large-area metasurfaces, the versatility of material choice allows for the nanoscale losses and subsequent heat generation to be spatially engineered. At the fundamental plasmonic mode, the incident electromagnetic energy is converted into localized surface plasmons confined to the metasurface resonators. These

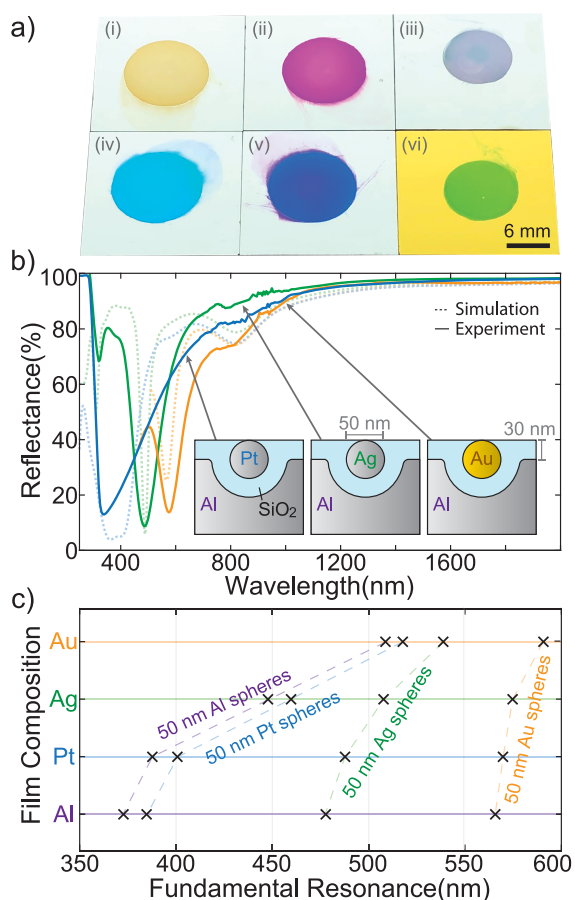


**Figure 3.** (a) Photographs of reflected light from select metasurfaces with resonances in the visible and UV region, where each metasurface is realized with 50 nm NPs, a 30 nm SiO<sub>2</sub> layer, and a 150 nm Al film unless otherwise noted. The metasurfaces are as follows: (i) Pt sphere; (ii) Ag sphere; (iii) Au sphere; (iv) Ag cube with 20 nm SiO<sub>2</sub>; (v) Ag cube; (vi) Au sphere with an Au film. (b) Experimental and simulated spectra for metasurfaces comprised of 50 nm spheres of various compositions along with their corresponding diagrams. (c) Depiction of various fundamental resonances achievable for various 50 nm NPs and film compositions as computed from simulations.

localized plasmons decay at femtosecond time scales and generate heat due to electron–phonon scattering on picosecond time scales.<sup>18–21</sup> The power loss density in this system in units of W/m<sup>3</sup> can be estimated classically via resistive/Ohmic losses due to the collective movement of charges (i.e., plasmon) in a lossy conductor.<sup>20</sup> The power loss density for the metasurface element,  $Q_h$ , is calculated from eq 1

$$Q_h(\vec{r}, \lambda) = \frac{c}{2\lambda} \cdot \epsilon''(\lambda) \cdot |\vec{E}(\vec{r}, \lambda)|^2 \quad (1)$$

where  $\vec{r}$  is the spatial location in the metasurface unit cell,  $c$  is the speed of light,  $\lambda$  is the wavelength,  $\epsilon''(\lambda)$  is the imaginary component of the permittivity, and  $\vec{E}(\vec{r}, \lambda)$  is the electric field vector. Intentional choices for the NP geometry and material composition allow for control over the spatial electric field distribution. With the design of this spatial electric field distribution and its relative placement in high-loss or low-loss materials, i.e. materials with high or low imaginary permittivities, the power loss density can be spatially engineered. For example, the spatial losses and subsequent heat generation can be controlled for a fixed geometrical design through the material choice, as seen in Figure 4a with 50 nm spheres of various

compositions. The power loss density,  $Q_h$ , is shown for five representative metasurface elements, where the spatial losses can be tuned between the 96% occurring in the NP with the Au NP/Ag film geometry to 96% occurring in the film with the Ag NP/Au film. The fractional absorption occurring within a specific region, denoted as  $A_{\text{region}}(\lambda)$ , can be calculated from eq 2

$$A_{\text{region}}(\lambda) = \frac{1}{A_{\text{total}}(\lambda)} \cdot \iiint_{\text{region}} Q_h(\vec{r}, \lambda) d\vec{r} \quad (2)$$

where  $A_{\text{total}}(\lambda)$  is the total absorption of the metasurface element, where the power loss density is integrated over the volume of the desired region, such as the NP, spacer, or film. Figure 4b demonstrates the fractional spectral absorption for an Au NP/Au film calculated with eq 2, where the fractional absorption for the film, NP, and spacer are shown. For wavelengths shorter than 500 nm, the interband transition of Au governs the large absorptions occurring in both the film and NP.<sup>18</sup> Past interband transitions, the fundamental plasmonic resonance dominates at 590 nm, showing a significantly enhanced absorption in the Au NP due to the electric field confinement in and around the NP. At the peak absorption of 99.8%, over 62% is absorbed in the Au NP and 38% in the Au film. Figure 4c shows the absorption percentages occurring in the NP and film for simulated metasurfaces at their resonance wavelengths. All of the simulated metasurfaces have the same geometry with a 24 nm SiO<sub>2</sub> spacer, but the NP and film material are varied among Au, Ag, Al, and Pt. The highest fraction of power absorbed in the NP occurs with an Au NP and an Ag film, showing 96% of all absorption occurring in the NP on resonance. The lowest fraction of power absorbed in the NP occurs with an Ag NP and an Au film, where 4% of all absorption occurs in the NP at its resonance. These two cases are shown pictorially in Figure 4a on the far left and far right images, where most of the absorption is either happening in the NP or film. By utilizing other material combinations, the relative absorption and subsequent heat generation in the metasurface can be spatially engineered for resonances spanning the UV to SWIR region.

The presented metasurface architecture leverages the strengths of colloidal synthesis, self-assembly, and large-area deposition processes to demonstrate nanometer- to millimeter-scale control of absorption processes from 330 to 2740 nm. Furthermore, the absorbing metasurfaces have promising spectral, environmental, and geometrical characteristics for filling a spectral niche for optical metasurfaces with feature sizes below the resolution of standard i-line photolithographic systems. The influence of NP shape and material composition were analyzed both by experiments and with finite-element simulations to show the flexibility of this method with various crystallinities, materials, shapes, and sizes. In particular, this flexibility allows for the heat or hot-electron generation within these metasurfaces to be consolidated closer to an active film or material, for a variety of hot-electron or photothermal processes. For instance, integration of a thermally sensitive film, such as a pyroelectric material, into the gap of the plasmonic nanocavity would allow for an optical–thermal–electrical conversion device for the creation of photodetectors<sup>22–24</sup> sensitive from the ultraviolet to short-wave infrared region. Incorporation of actively tunable materials into these metasurfaces would allow for dynamic control of their reflection spectra<sup>16,25–28</sup> for spectrally tunable photodetectors or beam-steering surfaces. The presented metasurfaces could provide a promising platform for a new generation of optical devices spanning the UV to SWIR region.

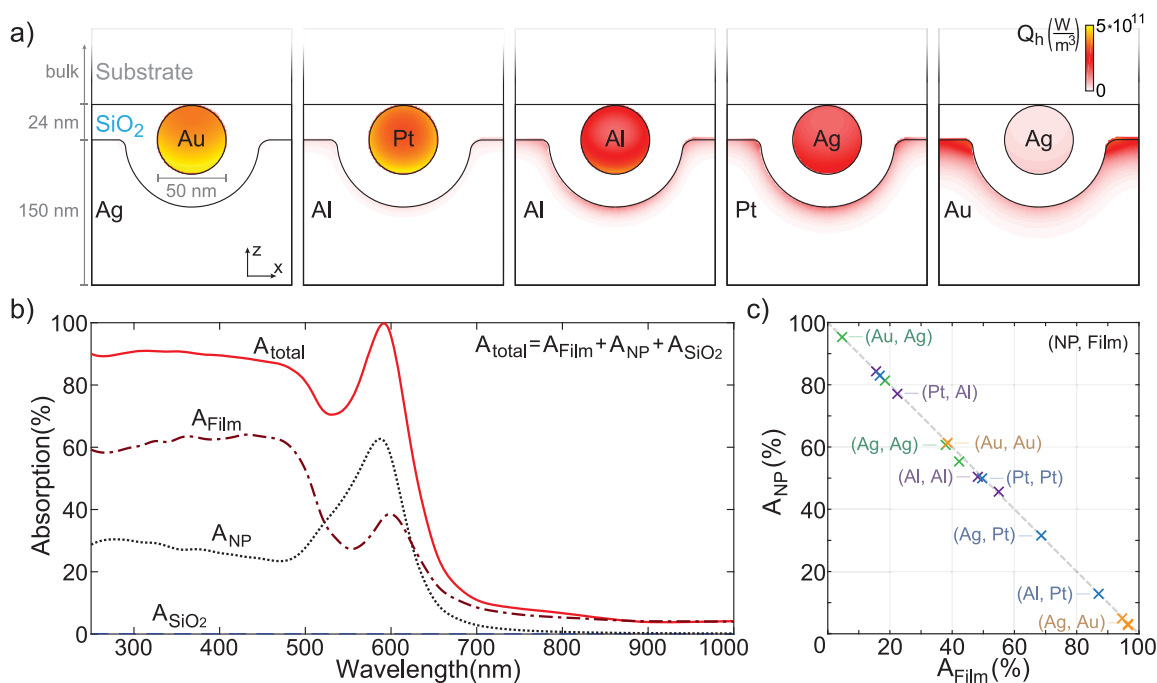


**Figure 4.** (a) Simulated absorbed power density of metasurface unit cells comprised of 50 nm spheres embedded in films with varied compositions, where the highest losses are shown in yellow and the lowest losses are shown in white. The losses can be engineered to occur in either the NP or film through alteration of their composition. (b) Simulated absorption spectra of a 50 nm Au sphere with an Au film along with the absorption spectra localized in each constituent material of the metasurface calculated according to eq 2. (c) Absorption percentage occurring in the NP and the film for metasurfaces comprised of 50 nm spheres, where the dashed line indicates 100% total absorption. This demonstrates that with only four plasmonic materials the fractional losses between the NP and the film can be engineered over nearly the full parameter space.

## METHODS

**Sample Fabrication.** First, a transparent substrate, in this case a VWR no. 2 coverslip, was cleaned in acetone and isopropyl alcohol. Next, a nanoscale adhesion layer was deposited using layer-by-layer dip coating of alternating polyelectrolyte (PE) layers composed of a positively charged poly(allylamine) hydrochloride (PAH) polymer and a negatively charged polystyrenesulfonate (PSS) polymer with layers of  $\sim 1$  nm thickness. The PE polymers were deposited by dip coating the substrate in a 1 M NaCl solution with 3 mM of PAH or PSS. After dip coating the samples were rinsed in a 1 M NaCl solution to remove residual polymer. The samples were rinsed with DI water and dried. The top layer, a positively charged PAH layer, was utilized to promote the adhesion of the colloidal nanoparticles to the surface due to the negatively charged PVP stabilizer coating. Next, the nanoparticles were deposited on the PE layers. For the initial experiments a variety of nanoparticles, including Ag nanocubes, Ag cuboctahedra, Au/Ag/Pt nanospheres, and silica–Au core–shell nanospheres, were self-assembled onto the PE layers. All nanoparticles used in this experiment were commercially synthesized (nanoComposix, Inc., San Diego). The solutions were prepared by concentrating a 1 mg/mL solution of nanoparticles and resuspending them in 18 M $\Omega$  DI water with a final concentration of 4 mg/mL. A coverslip with the final nanoparticle solution was inverted on the PE layers, often referred to as drop casting, and the cubes were allowed 1 h to settle and self-assemble onto the surface. During the nanoparticle deposition, the sample was placed in a refrigerator to reduce evaporation. Next, the samples were washed with DI water, removing excess nanoparticle solution, and were dried with nitrogen gas. Following the nanoparticle deposition, the SiO<sub>2</sub> and Si<sub>3</sub>N<sub>4</sub> dielectric spacer layers were

grown conformally around the nanoparticles with plasma-enhanced chemical vapor deposition (PECVD) at 200 °C. Other thin-film deposition techniques such as atomic layer deposition (ALD) or sputtering could also be utilized to form the spacer layer around the nanoparticles. After deposition of the dielectric layer, the nanoparticle/dielectric structure was surrounded in an optically thick metallic film of 150–250 nm thickness depending on the particle size. In this work, the metallic film consisted of Au or Al and was physically deposited with a DC sputtering machine.

**Reflection Measurements.** Reflection spectra of the samples were collected with a Shimadzu UV-3600 commercial spectrometer in normal reflectance mode. The spectra correspond to an integrated area of 5 mm in diameter and were normalized relative to coverslips with the same metallic film as the measured sample.

**Finite-Element Simulations.** The simulations were conducted in COMSOL Multiphysics utilizing the Wave Optics module for the absorptive characteristics and calculation of the power loss density. The electromagnetic (EM) simulation was conducted in the frequency domain with the boundary conditions shown in Figure S1, where periodic boundary conditions and perfectly matched layers were used to simulate an infinitely periodic array of the plasmonic resonators. The electric field enhancement and spatial loss density were calculated with the frequency domain simulation results. In the simulations, a range of fill fractions between 4 and 25% were used to ensure that the lattice mode was far removed from the plasmonic mode.

## ■ ASSOCIATED CONTENT

### SI Supporting Information

The Supporting Information is available free of charge at <https://pubs.acs.org/doi/10.1021/acs.nanolett.2c00761>.

Illustration of the simulated geometry, details of the fabrication process for creating metasurfaces via template stripping, SEM images, and reflectance data of metasurfaces created via template stripping (PDF)

## ■ AUTHOR INFORMATION

### Corresponding Author

**Maiken H. Mikkelsen** – Department of Electrical and Computer Engineering, Duke University, Durham, North Carolina 27708, United States; [orcid.org/0000-0002-0487-7585](https://orcid.org/0000-0002-0487-7585); Email: [m.mikkelsen@duke.edu](mailto:m.mikkelsen@duke.edu)

### Authors

**Jon W. Stewart** – Department of Electrical and Computer Engineering, Duke University, Durham, North Carolina 27708, United States

**Tamra Nebabu** – Department of Electrical and Computer Engineering, Duke University, Durham, North Carolina 27708, United States

Complete contact information is available at:

<https://pubs.acs.org/doi/10.1021/acs.nanolett.2c00761>

### Notes

The authors declare no competing financial interest.

## ■ ACKNOWLEDGMENTS

Support is acknowledged from the Office of Naval Research (ONR) award no. N00014-17-1-2589, the Army Research Office (ARO) award no. W911NF1610471, and the Air Force Office of Scientific Research (AFOSR) award nos. FA9550-18-1-0326 and FA9550-21-1-0312. J.W.S. also acknowledges support from the Department of Defense (DoD) through the National Defense Science & Engineering Graduate Fellowship (NDSEG).

## ■ REFERENCES

- (1) Lassiter, J. B.; McGuire, F.; Mock, J. J.; Ciraci, C.; Hill, R. T.; Wiley, B. J.; Chilkoti, A.; Smith, D. R. Plasmonic waveguide modes of film-coupled metallic nanocubes. *Nano Lett.* **2013**, *13*, 5866.
- (2) Akselrod, G. M.; Huang, J.; Hoang, T. B.; Bowen, P. T.; Su, L.; Smith, D. R.; Mikkelsen, M. H. Large-Area Metasurface Perfect Absorbers from Visible to Near-Infrared. *Adv. Mater.* **2015**, *27*, 8028.
- (3) Walter, R.; Tittel, A.; Berrier, A.; Sterl, F.; Weiss, T.; Giessen, H. Large-Area Low-Cost Tunable Plasmonic Perfect Absorber in the Near Infrared by Colloidal Etching Lithography. *Adv. Opt. Mater.* **2015**, *3*, 398.
- (4) Moreau, A.; Ciraci, C.; Mock, J. J.; Hill, R. T.; Wang, Q.; Wiley, B. J.; Chilkoti, A.; Smith, D. R. Controlled-reflectance surfaces with film-coupled colloidal nanoantennas. *Nature* **2012**, *492*, 86.
- (5) Zhao, J.; Jaber, S.; Mulvaney, P.; Braun, P. V.; Giessen, H. Repetitive Hole-Mask Colloidal Lithography for the Fabrication of Large-Area Low-Cost Plasmonic Multishape Single-Layer Metasurfaces. *Adv. Opt. Mater.* **2015**, *3*, 680.
- (6) Bowen, P. T.; Smith, D. R. Coupled-mode theory for film-coupled plasmonic nanocubes. *Phys. Rev. B - Condens. Matter Mater. Phys.* **2014**, *90*, 195402.
- (7) Alaei, R.; Albooyeh, M.; Rockstuhl, C. Theory of metasurface based perfect absorbers. *J. Phys. D: Appl. Phys.* **2017**, *50*, 503002.
- (8) Mkhitarian, V. K.; Ghosh, D. S.; Rude, M.; Canet-Ferrer, J.; Maniara, R. A.; Gopalan, K. K.; Pruneri, V. Tunable Complete Optical Absorption in Multilayer Structures Including Ge<sub>2</sub>Sb<sub>2</sub>Te<sub>5</sub> without Lithographic Patterns. *Adv. Opt. Mater.* **2017**, *5*, 1600452.
- (9) Baumberg, J. J.; Aizpurua, J.; Mikkelsen, M. H.; Smith, D. R. Extreme nanophotonics from ultrathin metallic gaps. *Nat. Mater.* **2019**, *18*, 668.
- (10) Bagheri, S.; Weber, K.; Gissibl, T.; Weiss, T.; Neubrech, F.; Giessen, H. Fabrication of Square-Centimeter Plasmonic Nanoantenna Arrays by Femtosecond Direct Laser Writing Lithography: Effects of Collective Excitations on SEIRA Enhancement. *ACS Photonics* **2015**, *2*, 779.
- (11) Gonçalves, M. R. Plasmonic nanoparticles: fabrication, simulation and experiments. *J. Phys. D: Appl. Phys.* **2014**, *47*, 213001.
- (12) Abedini Dereshgi, S.; Ghobadi, A.; Hajian, H.; Butun, B.; Ozbay, E. Ultra-Broadband, Lithography-Free, and Large-Scale Compatible Perfect Absorbers: The Optimum Choice of Metal layers in Metal-Insulator Multilayer Stacks. *Sci. Rep.* **2017**, *7*, 14872.
- (13) Ghobadi, A.; Hajian, H.; Butun, B.; Ozbay, E. Strong Light-Matter Interaction in Lithography-Free Planar Metamaterial Perfect Absorbers. *ACS Photonics* **2018**, *5*, 4203.
- (14) Ding, F.; Mo, L.; Zhu, J.; He, S. Lithography-free, broadband, omnidirectional, and polarization-insensitive thin optical absorber. *Appl. Phys. Lett.* **2015**, *106*, 061108.
- (15) Kats, M. A.; Blanchard, R.; Genevet, P.; Capasso, F. Nanometre optical coatings based on strong interference effects in highly absorbing media. *Nat. Mater.* **2013**, *12*, 20.
- (16) Kats, M. A.; Sharma, D.; Lin, J.; Genevet, P.; Blanchard, R.; Yang, Z.; Qazilbash, M. M.; Basov, D. N.; Ramanathan, S.; Capasso, F. Ultrathin perfect absorber employing a tunable phase change material. *Appl. Phys. Lett.* **2012**, *101*, 221101.
- (17) Li, Z.; Butun, S.; Aydin, K. Large-Area, Lithography-Free Super Absorbers and Color Filters at Visible Frequencies Using Ultrathin Metallic Films. *ACS Photonics* **2015**, *2*, 183.
- (18) Sykes, M. E.; Stewart, J. W.; Akselrod, G. M.; Kong, X.-T.; Wang, Z.; Gosztola, D. J.; Martinson, A. B. F.; Rosenmann, D.; Mikkelsen, M. H.; Govorov, A. O.; Wiederrecht, G. P. Enhanced generation and anisotropic Coulomb scattering of hot electrons in an ultra-broadband plasmonic nanopatch metasurface. *Nat. Commun.* **2017**, *8*, 986.
- (19) Zhu, X.; Vannahme, C.; Højlund-Nielsen, E.; Mortensen, N. A.; Kristensen, A. Plasmonic colour laser printing. *Nat. Nanotechnol.* **2016**, *11*, 325.
- (20) Kong, X. T.; Khosravi Khorashad, L.; Wang, Z.; Govorov, A. O. Photothermal Circular Dichroism Induced by Plasmon Resonances in Chiral Metamaterial Absorbers and Bolometers. *Nano Lett.* **2018**, *18*, 2001.
- (21) Spitzer, F.; Glavin, B. A.; Belotelov, V. I.; Vondran, J.; Akimov, I. A.; Kasture, S.; Achanta, V. G.; Yakovlev, D. R.; Bayer, M. Enhancement of electron hot spot relaxation in photoexcited plasmonic structures by thermal diffusion. *Phys. Rev. B* **2016**, *94*, 201118.
- (22) Ogawa, S.; Okada, K.; Fukushima, N.; Kimata, M. Wavelength selective uncooled infrared sensor by plasmonics. *Appl. Phys. Lett.* **2012**, *100*, 021111.
- (23) Suen, J. Y.; Fan, K.; Montoya, J.; Bingham, C.; Stenger, V.; Sriram, S.; Padilla, W. J. Multifunctional metamaterial pyroelectric infrared detectors. *Optica* **2017**, *4*, 276.
- (24) Stewart, J. W.; Vella, J. H.; Li, W.; Fan, S.; Mikkelsen, M. H. Ultrafast pyroelectric photodetection with on-chip spectral filters. *Nat. Mater.* **2020**, *19*, 158.
- (25) Hoang, T. B.; Mikkelsen, M. H. Broad electrical tuning of plasmonic nanoantennas at visible frequencies. *Appl. Phys. Lett.* **2016**, *108*, 183107.
- (26) Peng, J.; Jeong, H.-H.; Lin, Q.; Cormier, S.; Liang, H.-L.; De Volder, M. F. L.; Vignolini, S.; Baumberg, J. J. Scalable electrochromic nanoparticles using plasmonics. *Sci. Adv.* **2019**, *5*, No. eaaw2205.
- (27) Tittel, A.; Michel, A. K. U.; Schäferling, M.; Yin, X.; Gholipour, B.; Cui, L.; Wuttig, M.; Taubner, T.; Neubrech, F.; Giessen, H. A Switchable Mid-Infrared Plasmonic Perfect Absorber with Multi-spectral Thermal Imaging Capability. *Adv. Mater.* **2015**, *27*, 4597.

(28) Wilson, W. M.; Stewart, J. W.; Mikkelsen, M. H. Surpassing Single Line Width Active Tuning with Photochromic Molecules Coupled to Plasmonic Nanoantennas. *Nano Lett.* **2018**, *18*, 853.

## Recommended by ACS

### Reconfigurable Molecularization of Terahertz Meta-Atoms

Hyunseung Jung, Hojin Lee, *et al.*

APRIL 28, 2022  
ACS PHOTONICS

READ 

### Self-Assembled Nano-Lotus Pod Metasurface for Light Trapping

Nayeun Lee, Jonghwa Shin, *et al.*

MAY 19, 2021  
ACS PHOTONICS

READ 

### Color Routing via Cross-Polarized Detuned Plasmonic Nanoantennas in Large-Area Metasurfaces

Matteo Barelli, Francesco Buatier de Mongeot, *et al.*

MAY 13, 2020  
NANO LETTERS

READ 

### TiO<sub>2</sub> Nanodisk Arrays as All-Dielectric Huygens' Metasurfaces for Engineering the Wavefront of Near-UV Light

Tse-An Chen, Ta-Jen Yen, *et al.*

DECEMBER 27, 2021  
ACS APPLIED NANO MATERIALS

READ 

Get More Suggestions >